International Forum on Aeroelasticity and Structural Dynamics
IFASD 2024
17-21 June 2024, The Hague, The Netherlands

LIMIT CYCLE OSCILLATION OF A PLATE WITH PIEZOELECTRIC ELEMENTS IN SUPERSONIC FLOW

Maxim Freydin[1], Luisa Piccolo Serafim[2], Earl H. Dowell[2], Santosh Vaibhav Varigonda[3], Venkateswaran Narayanaswamy[3]

[1]Technion – Israel Institute of Technology
3200003, Haifa, Israel
freydinmaxim@technion.ac.il

[2]Duke University
27708, Durham, NC

[3]North Carolina State University
27695, Raleigh, NC

Keywords: Flutter, supersonic, limit cycle oscillation, pressure sensitive paint, elastic plate, acoustic pressure

Abstract: Fluid structure interaction of an elastic plate with piezoelectric elements, turbulent freestream flow at Mach 2.5, and a pressurized cavity is investigated computationally and correlated with a recent experiment. The pressure field on the surface of the plate is measured using pressure sensitive paint and the structural response is observed using the measured voltage of a piezoelectric patch. The pressure and structural response are investigated in terms of frequency content and amplitude variation over time. The measurements show a dominant frequency of oscillation which indicates the likely onset of flutter and a post-flutter limit cycle oscillation (LCO). A computational investigation is conducted to study the effects of static pressure differential, temperature differential, cavity pressure coupling, and plate boundary conditions on the linear flutter onset condition and the nonlinear post-flutter LCO characteristics. Rivets that connect the plate to the supporting structure are modeled as local constraint in the in-plane direction and their effect on the nonlinear stiffness is investigated. The measured plate natural frequencies outside of the wind tunnel are shown to be closer to pinned than to clamped boundary conditions. Computations show that the coupling between the cavity acoustic and plate structural modes is necessary for flutter onset in the wind tunnel conditions. Direct correlation between computed and measured aerodynamic pressure shows reasonable agreement in amplitude and frequency. Computational results are obtained using Piston Theory and also potential flow aerodynamics, which is more appropriate for the reduced frequency on the order of 1 considered in this work. Lastly, computed and measured pressure LCO mode shapes are extracted and correlated using the spectral proper orthogonal decomposition[1].

[1]This paper has also been submitted for publication to the AIAA Journal.

NOMENCLATURE AND ABBREVIATIONS

a	=	plate length, m
a_c	=	cavity fluid speed of sound (with subscript), m/s
b	=	plate width, m
p_∞	=	freestream static pressure, Pa
$p_c(x,y,z,t)$, $p_{c,ref}(t)$	=	cavity static pressure (perturbation, reference), Pa
w, u, $v(x,y,t)$	=	physical displacement components, m
w_i, u_i, $v_i(t)$	=	i-th modal displacement coordinates, m
$K(x,y)$	=	distributed in-plane boundary stiffness, $\mathrm{N/m^2}$
$K_{BC} = Ka/Eh$	=	non-dimensional in-plane boundary stiffness
$P_i(t)$	=	i-th modal cavity pressure coordinate, Pa
$\psi_i^w, \psi_i^u, \psi_i^v(x,y)$	=	i-th basis function for $w, u, v(x,y,t)$
$\psi_i^c(x,y,z)$	=	i-th basis function for $p_c(x,y,z,t)$
$\Delta T = T(x,y,t) - T_{support}$	=	temperature differential, K
$\Delta p_s = p - p_{c,ref}$	=	static pressure differential, Pa
BL	=	Boundary layer
PSP	=	Pressure sensitive paint
LPT	=	Linear Piston Theory Aerodynamics
PF	=	Potential Flow Aerodynamics
RMS	=	Root-mean-square
MM	=	Moving-mean
STFT	=	Short-time Fourier transform
SSSS	=	Simply supported (pinned) boundary conditions
CCCC	=	Clamped boundary conditions
SPOD	=	Spectral Proper Orthogonal Decomposition
u/s, d/s	=	Upstream, downstream

1 INTRODUCTION

Elastic plates in supersonic flow is a fluid-structure interaction problem that has been the focus of a range of theoretical, computational, and experimental studies in recent years. Plates and shells are used as structural elements in aerial vehicles where the aeroelastic response depends on the local freestream conditions on the vehicle structure as well as the flight trajectory [1, 2]. At certain freestream conditions, plates and shells may experience flutter and post-flutter limit-cycle oscillation (LCO) which is a nonlinear phenomenon and in many cases not immediately destructive to the structure [3]. Accurate prediction of frequency, amplitude and the spatial shape of the aeroelastic LCO is important for the design of low-weight reusable structures and preventing fatigue failure [4]. The focus of this work is the response of a thin elastic plate at Mach 2.5 considered in a recent experimental study [5], which as will be shown, exhibited post-flutter LCO near the edge of flutter envelope.

Until recent years, the focus of wind tunnel experiments conducted in the context of aeroelasticity with elastic plates was predominately concerned with instability onset [6–8]. Results of these experiments were used to validate and calibrate theoretical and computational models. With the advance of diagnostic capabilities, especially in full-field pressure and displacement measurements, researchers shifted their focus and stepped beyond the flutter onset envelop. With this in mind, it is timely to examine and extend existing computational tools for accurate

characterization and prediction of LCO which involves structural nonlinearity. The following is a brief review of important works in which high sampling rate diagnostics were used to investigate the post-flutter, post-buckling, and in some cases the likely combination of the two, response of elastic plates.

In a recent experimental study, Daub et al. [9] measured the post-flutter LCO response of an elastic plate at Mach 5.3. They showed static buckling due to aerodynamic heating in pre-flutter conditions, post-flutter LCO response with heating to post-buckling temperature, and a case of sudden stabilization. The smallest thickness considered was 0.3 mm for which a LCO amplitude of up to 3 mm was reported. Nonlinear stiffness in thin plates becomes important when the ratio between displacement and thickness is of order 1 [3], and in this study a value of 10 was measured. This suggest that the response was dominated by a structural nonlinearity and that the structure was under freestream conditions significantly beyond flutter onset. An experimental study by Spottswood et al. [4] showed the transient response of an elastic plates at Mach 2 with hot flow reaching a stagnation temperature of 390K during the supersonic wind tunnel start. The plate displacement showed flutter onset, reaching of LCO, and stabilization due to buckling which was supported by a related computational study [10]. The nondimensional displacement in this experiment reached values of between 1 and 2 while the computations produced larger values by a factor of up to 2.

Brouwer et al. [11] measured chaotic and periodic LCO responses at Mach 2 using full-field displacement and pressure measurement techniques. Experimental configuration and facility was as in [4] however the work extended to study the effect of cavity pressure and shock impingement on the fluid-structure response. Post-flutter LCO amplitudes of up to 3 were measured. In a subsequent computational work [12], Brouwer et al. used an in-house finite element structural model with Piston Theory aerodynamics enriched with the steady-state fluid field from a Reynolds-averaged Navier-Stokes (RANS) solution. The correlation between computations and experiment showed good agreement for cases with an attached boundary layer. With a stronger impinging shock and boundary layer separation, frequency content and amplitudes differences between computation and experiment grew. A more recent experimental study by Brouwer et al. [13] showed additional experimental results with impinging shock, boundary layer separation, and post-flutter LCO response with an amplitude of up to 3 plate thicknesses.

Other researchers measured elastic oscillation of plates in high-speed flows with smaller nondimensional amplitudes. Currao and He [14] used point displacement laser sensors to measure the oscillation of a plate at transonic speeds. Whalen et al. [15] considered a plate mounted on a shock ramp and while the amplitude of the dynamic oscillation was small, aerodynamic heating led to a static deflection at the center of approximately 1 plate thickness. Eitner et al. [16] measured the response of a thin compliant plate positioned upstream of a compression ramp at Mach 2 however no indication of significant FSI coupling was found suggesting the plate was far from flutter onset. Daub et al. [17] measured the response of a plate at Mach numbers 3 and 4 under a moving impinging shock however the oscillation amplitude was relatively small. Gramola et al. [18] measured the full-field deformation of a plate at Mach numbers 1.4 and 2 with different impiniging shock configuration and static pressure differential by controlling the cavity pressure. However deformation was measured at a relatively low rate of 100 Hz and average deformation shapes were shown to reach a displacement of up to 5 thicknesses.

The present paper is organized as follows. In Section 2, the theoretical-computational model of a plate, aerodynamic pressure, and acoustic cavity are described. In Section 3, the wind tunnel

experiments [5] are described and computations are correlated with bench tests outside of the wind tunnel. In Section 4 results of stability and post-flutter transient analyses are presented and correlated with experiment.

2 THEORETICAL MODEL

Figure 1 shows the top and side views of the aeroelastic test article. The article consists of an elastic plate with two piezoelectric patches, labeled upstream (u/s) and downstream (d/s), an incoming supersonic freestream flow on one side, and a closed cavity on the other. The piezoelectric patches are assumed to be bonded ideally to the plate on its lower side. In the computational model, the plate is considered with either clamped or pinned (simply-supported) transverse edge connections and with distributed in-plane springs around the edges. The upper surface of the plate interacts with the incoming flow which affects the local static pressure, i.e. aerodynamic response. The plate has a temperature distribution ΔT which in this work decreases over time due to the relatively low stagnation temperature of the flow and it is assumed uniform across the plate. The differential between the temperature of the plate and the temperature of the rigid support structure creates an in-plane thermal stress. On the lower surface of the plate there is a closed cavity with an acoustic pressure component p_c due to the interaction of the non-convecting fluid and the elastic plate. The plate is also under the load of a static pressure differential, $\Delta p_s = p_\infty - p_{c,ref}$, which is independent of the plate motion.

In this work, the model derived in [19] is used however the in-plane boundary elasticity is modified to add the effect of local elasticity at the rivets. In addition, unsteady Potential Flow (PF) aerodynamics as formulated in [20] is implemented and compared with linear Piston Theory (LPT) aerodynamics. The PF aerodynamic model is expected to be more accurate at lower Mach numbers and reduced frequencies of order one [3] than LPT, which is the case in the present experiment.

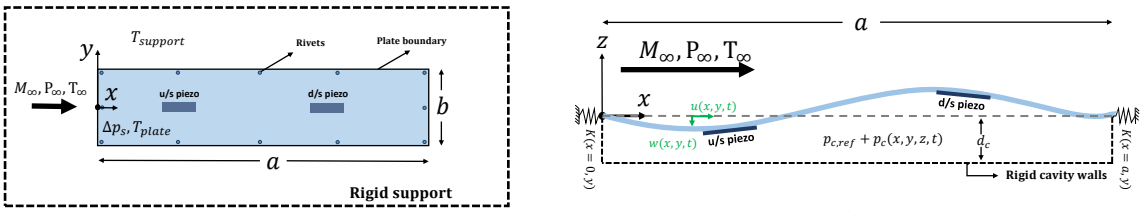

Figure 1: (a) Top and (b) side views of the elastic plate with two piezoelectric patches, freestream flow, cavity, static pressure differential, in-plane edge stiffness $K(x,y)$, rivets, and support and plate temperatures.

2.1 Plate model with rivets, cavity acoustics, and aerodynamics

A computational-theoretical model is derived in modal coordinates for the transverse plate displacement and the pressure perturbation inside the cavity according to Equation 1

$$w = \sum_i^{N_w} \psi_i^w(x,y) w_i(t) \tag{1a}$$

$$p_c = \sum_i^{N_c} \psi_i^c(x,y,z) P_i(t) \tag{1b}$$

The coupled governing system is shown in Equation 2 with the various fluid-structure terms identified and underlined (NL = nonlinear).

$$\begin{aligned}&\underbrace{M_{nk}\ddot{w}_k + \bar{C}_{nk}\dot{w}_k + G^{(1)}_{nk}w_k + \Delta T G^{(3)}_{nk}w_k}_{\text{linear plate model}} + \underbrace{D^{(2)}_{nkrs}w_k w_r w_s}_{\text{NL structural stiffness}} \\ &+ \underbrace{Q^{LPT/PF}_n(w,\dot{w})}_{\text{aerodynamic pressure}} - \underbrace{L^c_{kn}P_k}_{\text{cavity coupling}} + \underbrace{Q^s_n}_{\text{static pressure differential}} = 0\end{aligned} \tag{2a}$$

$$\underbrace{\rho_c L^c_{nk}\ddot{w}_k}_{\text{plate coupling}} + \underbrace{\frac{1}{a_c^2}M^c_{nk}\ddot{P}_k + C^c_{nk}\dot{P}_k + K^c_{nk}P_k}_{\text{acoustic wave eqn.}} = 0 \tag{2b}$$

The mass of piezoelectric elements is included in the calculation of the modal mass matrix M_{nk}. Temperature differential ΔT is assumed uniform and prescribed in transient and eigenvalue solutions. The effect of elastic in-plane boundary conditions is included through the calculation of the linear thermal stiffness $G^{(3)}_{nk}$ and the nonlinear stiffness $D^{(2)}_{nkrs}$. The aerodynamic pressure $Q^{LPT/PF}_n(w,\dot{w})$ is considered as LPT or PF and their exact form is detailed below. However they are both a function of modal displacement and velocity. For a detailed formulation and derivation of the different terms the reader is referred to [19].

An important modification is made to the structural model of the elastic edges in the in-plane direction (see Figure 1). In previous work [19], the elastic component was considered along the full length of the four edges. However for the present study a plate was designed and manufactured with discrete rivet connections to the supporting structure as shown in Figures 1 and 2. A similar experimental configuration was considered in [17] and the importance of adding rivets to the computational finite-element model was demonstrated. Rivets carry shear in-plane loads which in this structural model is represented by the in-plane boundary restraint. To account for the elastic energy due to rivets at discrete locations the in-plane stiffness terms are calculated as follows

$$\begin{aligned}K^u_{ik} &= \sum_{r_y}\left\{\int_{y^s_r}^{y^e_r} K\left[(\psi^u_i\psi^u_k)|_{x=0} + (\psi^u_i\psi^u_k)|_{x=a}\right]dy\right\} \\ K^v_{ik} &= \sum_{r_x}\left\{\int_{x^s_r}^{x^e_r} K\left[(\psi^v_i\psi^v_k)|_{y=-b/2} + (\psi^v_i\psi^v_k)|_{y=b/2}\right]dx\right\}\end{aligned} \tag{3}$$

Where the summation over indices r_x and r_y represents the number of rivets along each pair of edges. The above formulation assumes symmetrical rivet placement for each pair of edges. The limits of integration determine the effective length of the restraint.

2.2 Linear Piston Theory and Potential Flow aerodynamics

Two aerodynamic models are considered: (1) first order linear Piston Theory (LPT) and (2) Potential Flow (PF) aerodynamics. Both forms can be derived from the linear potential flow equations [3] which is applicable for small displacements typical to plates and shells. However LPT is obtained in the limit of high Mach number and any reduced frequency or for any Mach number for high reduced frequencies. The following Equation shows the aerodynamic stiffness and damping terms of LPT

$$Q^{PT}_n = A^{\dot{w}}_{nk}\dot{w}_k + A^{w}_{nk}w_k \tag{4}$$

As will be shown in the results section, the dominant reduced frequency in the current problem is of order one while the Mach number is 2.5. These parameters might be considered outside the range of LPT applicability. To address this, the PF is used for most of this work (except for the eigenvalue approach solutions) and selected comparisons with LPT are made. The following is the aerodynamic terms for PF which includes the LPT stiffness and damping with the added memory effects represented by the time convolution integrals

$$Q_n^{PF} = A_{nk}^{\dot{w}}\dot{w}_k + A_{nk}^{w}w_k + \int_0^t I_{nk}(t-\tau)\dot{w}_k(\tau)\,d\tau + \int_0^t H_{nk}(t-\tau)w_k(\tau)\,d\tau \tag{5}$$

Detailed formulation and derivation can be found in [3] and [20]. Also see [21].

2.3 Solving the coupled fluid-structure system

Equation 2 shows a system of second order ordinary differential equations in time of size $N^w + N^c$. The unknowns are the modal coordinates w_n and P_n with their respective initial conditions provided. Two solution methods are used in the present work: (1) eigenvalue approach for stability and modal parameters analysis and (2) direct time-marching to obtain the transient and LCO characteristics. In both cases, 12 chordwise and 2 spanwise (symmetrical) bending structural modal coordiantes are used. The nonlinear stiffness and linear thermal stiffness terms are calculated using 20 chordwise and 20 spanwise in-plane displacement modes (u_n and v_n). For the cavity acoustic pressure, 10 chordwise, 2 spanwise and 1 depth modes are used.

For both solution methods, the system in Equation 2 is reduced to first order differential equation in time by defining a stacked vector, $\bar{y}$ of modal coordinates as follows

$$\bar{y} = \begin{Bmatrix} \bar{w} \\ \dot{\bar{w}} \\ \bar{P} \\ \dot{\bar{P}} \end{Bmatrix} \tag{6}$$

In the eigenvalue approach, Equation 2 is linearized in terms of the modal displacement of w_n to account for an optional initial static deformation w_n^s (e.g., due to Δp_s) which involves the nonlinear terms. Lastly, a small amplitude harmonic solution is assumed as follows

$$\bar{y} = \hat{y}e^{\omega t}, \quad \omega = \zeta\omega_R + \omega_R i \tag{7}$$

Solving the eigenvalue problem produces $2 \times (N_w + N_c)$ eigenvectors $\hat{y}$ and eigenvalues ω which can be decomposes into the natural frequency and modal damping as shown in Equation 7. The eigenvalues appear as conjugate pairs because the mass and stiffness matrices are real valued and the number of equations is even. The eigenvalues with non negative frequencies are selected and thus $N_w + N_c$ eigenvalues and eigenvectors remain. Note that zero frequencies are kept as they may represent the cavity Helmholtz mode, which is analogous to a rigid body motion mode, and possible statically unstable elastic modes due to buckling or divergence. In the present work, the LPT aerodynamic model is used in all solutions obtained using the eigenvalue approach.

The time marching solution is obtained by reformulating Equation 2 in terms of the stacked vector of coordinates in Equation 7. The convolution integrals in Equation 5 are implemented by obtaining the convolution kernels I_{nk} and H_{nk} at discrete time points and using linear interpolation to evaluate intermediate values. The ordinary differential system of equations is solved

using MATLAB's ode45 solver which is of the Runge-Kutta family with an adaptive time step. The convolution integral is truncated at a preset time window determined by the decaying value of the kernels.

For direct correlation of measured and computed aerodynamic pressure, the generalized aerodynamic force is transformed to physical pressure after the time marching solution is obtained. The PF aerodynamic generalized force $Q_n^{PF}(t)$ is transformed to pressure in physical coordinates $p^{PF}(x, y, t)$ as follows. First, recall that the generalized force is defined as the integral over the plate area of the physical pressure times the modal n-th modal coordinate

$$Q_n^{PF} = \iint p^{PF} \psi_n^w \, dx \, dy \tag{8}$$

Next, we assume the aerodynamic pressure in physical coordinates can be represented in the same modal basis as the displacement w

$$p^{PF} = \sum_i^{N_w} \psi_i^w(x, y) P_i^{PF}(t) \tag{9}$$

Substitute Equation 9 into Equation 8

$$Q_n^{PF} = \iint \psi_i^w P_i^{PF} \psi_n^w \, dx \, dy = \bar{M}_{ni} P_i^{PF} \tag{10}$$

In the last transition the structural mass is identified (without scaling for the material properties) which generally is not diagonal. Finally, P_i^{PF} is obtained by inverting the mass matrix and the pressure in physical coordinates is obtained using Equation 9.

Piezoelectric elements used in this work produce voltage when they experience strain which can be related to the deformation of the plate. Similar to aerodynamic pressure, the piezoelectric voltage is calculated after a time marching solution is obtained using the following relation

$$V_c = V_i^u u_i + V_i^v v_i + V_i^w w_i + V_{ik}^{ww} w_i w_k + V_i^T T_i \tag{11}$$

Formulation and derivation details can be found in [22].

3 WIND TUNNEL EXPERIMENTS AND BENCH-TESTS

3.1 Wind tunnel facility and the test article

The experiments were conducted in the variable Mach number blowdown supersonic wind tunnel at North Carolina State University with a $150\,\mathrm{mm} \times 150\,\mathrm{mm} \times 650\,\mathrm{mm}$ test section. While the facility can be operated between Mach 1.6 - 4.0, the Mach number was set to 2.5 for this study. The test run lasted 10 seconds including the transient start and finish while the stable conditions were maintained for 8 seconds. The freesteram conditions are shown in Table 1.

The test article consisted of an elastic plate manufactured from an Aluminum sheet with nominal dimensions of $305\,\mathrm{mm} \times 90\,\mathrm{mm} \times 0.5\,\mathrm{mm}$. The thin sheet was riveted to a supporting structure as shown in Figure 2 creating a closed cavity on one side and with the other side exposed to the freestream flow. The effective dimensions of the plate fixed by rivets and material properties are shown in Table 2. Two piezoelectric elements were attached to the inner surface of the plate with properties and geometry listed in Table 2. The voltage of the downstream piezoelectric element is measured at 100 kHz and downsampled to 10 kHz to investigate the structural response of the plate. Pressure sensitive paint (PSP) is used to measure the pressure field on the plate surface at a rate of 10 kHz. For more details on the experimental configuration and measurements see [5].

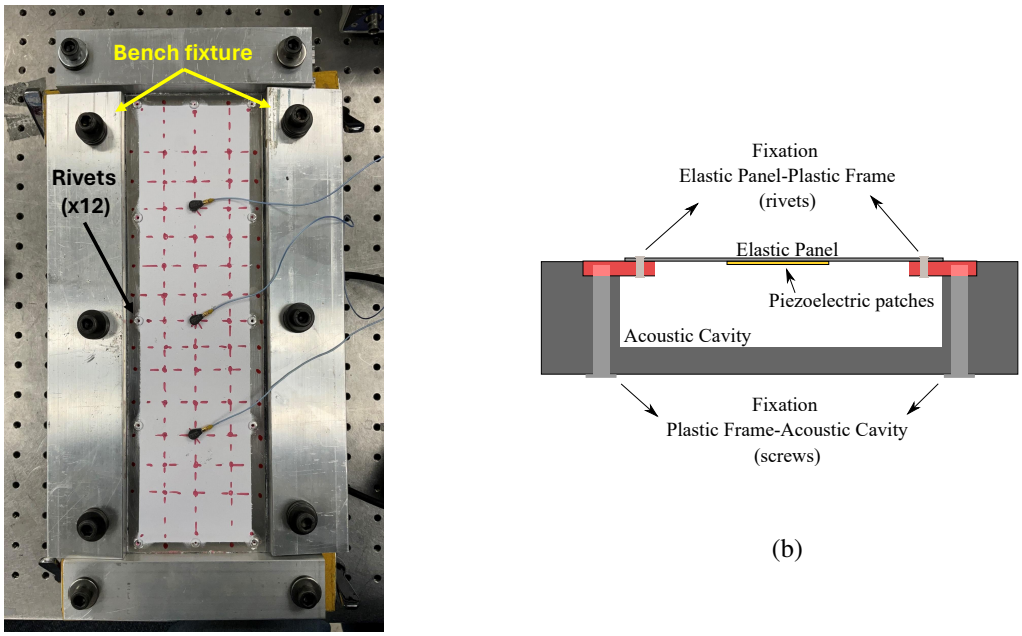

(a)

(b)

Figure 2: (a) Elastic plate fixed to a test bench during impact hammer tests (freestream side is shown) and (b) schematic of the plate connection to the 3D-printed plastic frame (red) using screws (light gray) inserted from the bottom into the steel support (gray) and up to the plastic frame.

Table 1: Freestream and cavity parameters

Parameter	Value
Freestream Mach, M_∞	2.5
Freestream speed, $U_\infty\,(m/s)$	574
Freestream static pressure, $p_\infty\,(\mathrm{kPa})$	26.33
Reynolds number, $Re_x\,(1/\mathrm{m})$	5.3×10^7
Stagnation temperature, $T_0\,(\mathrm{K})$	295
Cavity nominal pressure, $p_{c,ref}\,(\mathrm{kPa})$	32.4
Static pressure differential, $\Delta p_s = p_\infty - p_{c,ref}\,(\mathrm{kPa})$	-6.07
Cavity temperature, $T_c\,(\mathrm{K})$	295

3.2 Natural frequencies - bench tests

Modal bench testing was conducted for the plate with piezoelectric elements and cavity structure shown in Figure 2 using the roving hammer method with three accelerometers. Figure 3 shows the experimental and computed results for the first 8 natural frequencies. The computed results are shown for clamped and pinned transverse boundary conditions in four different configurations that include with/without cavity coupling and with/without added mass of two piezoelectric elements. The cavity fluid parameters used for this calculation are for air in room conditions. Results also include the theoretical natural frequencies of the cavity for the first two modes (horizontal dashed lines) without coupling to the plate.

The first five natural frequencies in Figure 3 show good agreement between theory and experiment for the pinned boundary conditions. Computational results also show that the clamped plate is more sensitive to the piezoelectric elements mass than the pinned plate which may reduce the natural frequencies of the first two modes by more than $100Hz$. The effect of the

Table 2: Material and geometrical properties of the plate and piezoelectric patches

Parameter	**Value**
Material	Aluminum
Modulus of elasticity, E (GPa)	68
Density, ρ_m (kg/m^3)	2700
Poisson's Ratio, ν	0.33
Coefficient of thermal expansion, α $(1/K)$	$24 \cdot 10^{-6}$
Length, a (mm)	292
Width, b (mm)	76.2
Thickness , h (mm)	0.5
Cavity depth , d_c (mm)	38.1
Piezo. Patch Model	Q220-A4BR-1305YB
Modulus of elasticity, E_p (GPa)	68
Density (mean, total mass of 2.3 gr), ρ_p (kg/m^3)	11166
Piezo. Patch Length, a_p (mm)	31.8
Piezo. Patch Width, b_p (mm)	12.7
Piezo. Patch Thickness , h_p (mm)	0.51
Upstream patch center location , $x_s^{u/s}/a$	0.25
Downstream patch center location , $x_s^{d/s}/a$	0.7

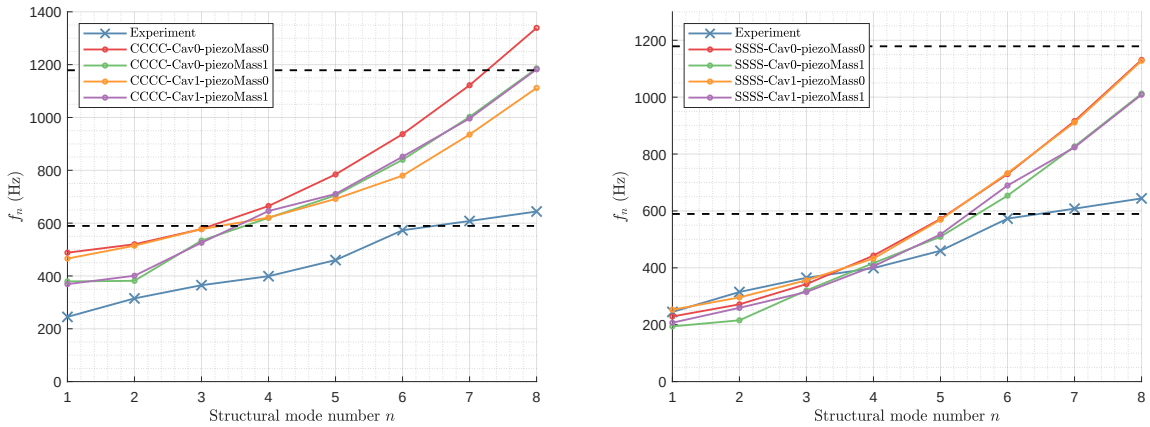

(a) (b)

Figure 3: Computed natural frequencies of a plate with (a) clamped and (b) pinned edges, with and without cavity coupling at room condition (Cav0/1), with and without piezo mass (piezoMass0/1). The first two cavity modes are shown in nominal form (without coupling to the plate). The experiment was conducted with cavity and piezoelectric elements.

cavity on the flat plate natural frequencies in room conditions is relatively small. However there is an important point to clarify with regard to cavity and plate modes. When we solve the coupled eigenvalue problem for the plate and cavity dynamics, the resulting eigenvalues and eigenvectors contain a mixture of natural frequencies and mode shapes of the coupled plate-cavity system. In Figure 2 the computational results for the structural modes were isolated by looking at the mode shapes and removing modes with dominant participation of cavity dynamics. This process was done manually and the threshold to determine which mode is dominant was not always clear. However there are only two cavity modes in the range of up to $1400Hz$ and any error created by a wrong selection leads to an error of approximately $\pm 50Hz$ in natural

frequency. The experimental results, on the other hand, do not contain separate information about the cavity modes and so the measured frequencies are likely to include a cavity mode around $600Hz$. The measured mode number 6 is possibly a cavity mode and if we omit it and shift modes number 7 and 8 one index to the left, the error between theory and experiment is reduces to the range of $\pm 20\%$ as is observed for the first five modes.

In the wind tunnel experiment, the plate is under a static pressure differential which leads to static deformation on the order of the plate thickness and the contribution of nonlinear stiffness. This effect is highly sensitive to the in-plane boundary conditions [10,19]. In the present experiment, the plate is connected to the supporting structure using rivets which is different than many previous works. To investigate the effect of in-plane boundary conditions on the contribution of nonlinear stiffness, two theoretical formulations are considered. In the first, in-plane elasticity is considered as distributed elasticity at the locations of the rivets according to Equation 3. A radius of 3 mm is considered for the rivets including those located in the corners. In the second formulation, edge elasticity is distributed along the full edge as considered in the authors' previous work [19]. Figure 4 shows results for both formulations with different values of non-dimensional in-plane stiffness and the freestream and cavity conditions inside the wind tunnel. Note that the in-plane boundary conditions have no effect on the results in 2 because the plate was flat. Figure 4(a) shows that for the two smallest values of K_{BC}, the natural frequencies of a statically deformed plate are almost identical. Only at the highest considered value is a change observed where the frequencies increase at lower order modes and decrease at the higher order modes. In Figure 4(b) where the elasticity is along the full edge it is seen that the natural frequencies are sensitive to K_{BC} and all three values show variation in the natural frequencies. Interesting to note is that for $K_{BC} = 100$, both in-plane boundary models show similar results for the natural frequencies. The configuration with the rivets in this case becomes similar to a case with fixed edge points in the in-plane direction which approximately similar to the case of a full fixed edge. The figure also shows the dominant frequency measured in the wind tunnel which is slightly lower than the first two natural frequencies of the coupled system with small values of K_{BC}. Following these results, all computations from this point will be for the pinned plate with in-plane elasticity at the rivets and $K_{BC} = 1$.

4 RESULTS AND DISCUSSION

In this section computational results are presented and correlated with the wind tunnel experiment. Figure 5 shows the short-time Fourier transform (STFT, absolute value squared is plotted) of the measured pressure (PSP, detrended component normalized by instantaneous moving-mean) at the plate center and the voltage of the downstream piezoelectric element (detrended component normalized by instantaneous moving-mean). All STFTs are calculated using a window size of 0.5 seconds, an overlap of 0.495 seconds, and a sampling rate of 20 kHz. Figure 5 shows a dominant harmony at 325 Hz in both signals with an approximately constant amplitude. This is in contrast to authors' previous work [22] where a steel plate responded with small amplitude oscillation and a wide range of participating structural modes in the range of 900 Hz and 3000 Hz. Without a direct measurement of displacement oscillation amplitude, the frequency content of the response is the strongest indicator for post-flutter LCO in this experimental campaign.

The following results are organized as follows. First, a linear stability analysis is presented and the effects of static deformation and cavity coupling are discussed. Next, transient computations show the sensitivity of the LCO amplitude to the static pressure differential. And lastly, transient simulations are presented with direct correlation with experiment.

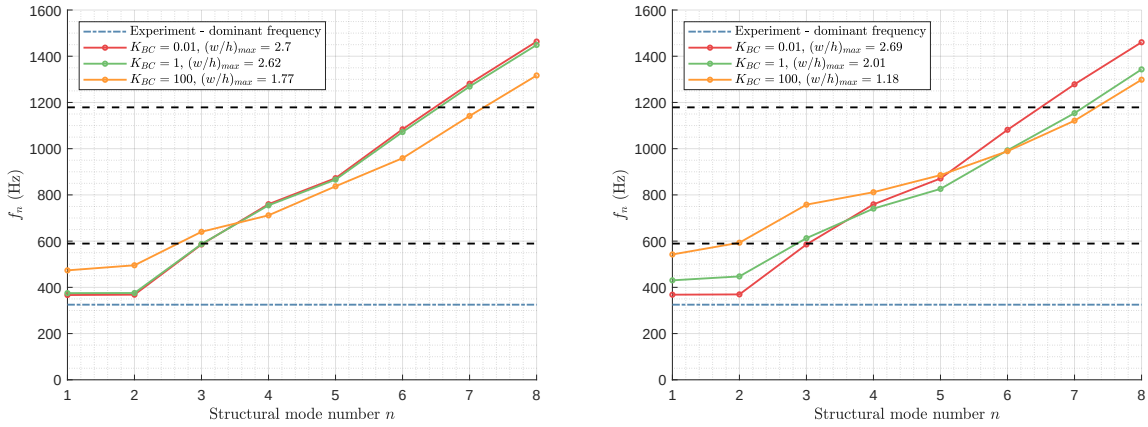

(a) (b)

Figure 4: Natural frequencies of a plate with pinned edges and in-plane edge stiffness modeled as (a) local elasticity only at the rivets position and (b) elasticity along the full edge. Cavity and Piston Theory aerodynamics coupling to the plate is considered at wind tunnel test conditions. The plate is deformed due to static pressure differential leading to nonlinear added stiffness (maximum displacement is shown in the legend). The added mass due to two piezoelectric elements is considered. The first two cavity modes are shown in nominal form (without coupling to the plate). Experiment (wind tunnel) - dominant frequency of oscillation observed in the measured pressure and piezo voltage.

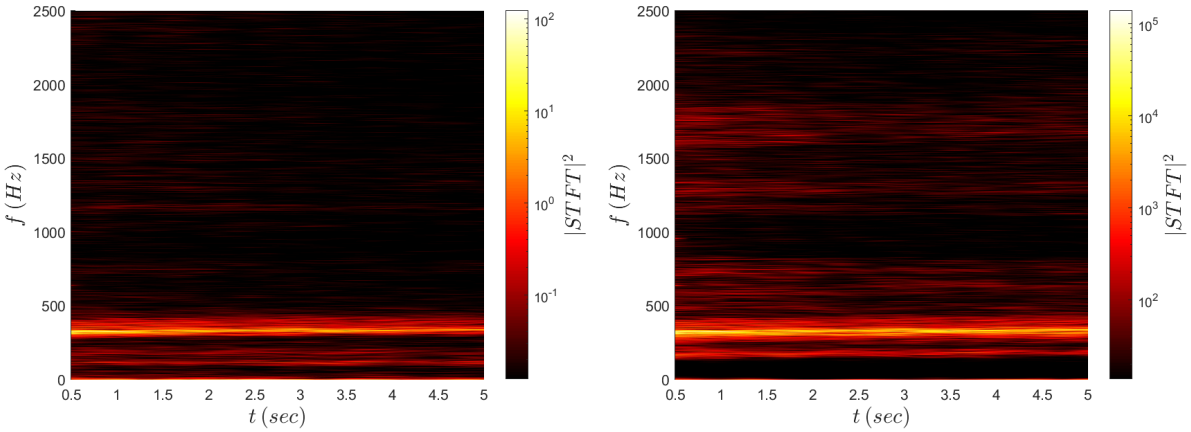

(a) (b)

Figure 5: Experimental data - (a) pressure sensitive paint (normalized by moving-mean) at the plate center and (b) downstream piezoelectric element voltage (normalized by moving-mean) short-time Fourier transforms.

4.1 Flutter analysis

Flutter analysis is conducted using the linear eigenvalue method as described in Section 2.3. Through the rest of this work, results are presented for pinned edges with in-plane boundary conditions modeled as rivets with a parameter of $K_{BC} = 1$ following the conclusions from Section 3.2. Figure 6 shows stable and flutter regions in the static pressure differential and temperature differential plane. The dashed line shows the approximate wind tunnel test trajectory. The temperature differential range was determined by measuring the plate temperature before and after the wind tunnel test. The static pressure differential is the difference between the static pressure of the freestream flow and the cavity reference pressure. Both pressures vary (modestly) over time in the wind tunnel experiment and the shown value is an approximation. As will be shown in the following results, the plate stability and post-flutter dynamics are highly

sensitive to static pressure differential in this range.

Figure 6(a) shows the number of unstable modes where zero means the plate is stable. It is shown that for a relatively small change in Δp_s the unstable response may show a qualitative change, e.g., by exhibiting more than a single dominant frequency during LCO. Figure 6(b) shows the frequency of the unstable mode that has the largest value of negative damping. The lowest flutter frequency is found to be around 355 Hz, which is close to the peak oscillation energy found experimentally and shown in Figure 5. This lowest frequency is due to first and second mode coalescence flutter. However for Δp_s smaller than $-6kPa$, the dominant unstable mode switches to $595Hz$ which is due to cavity and plate mode coupling. Even higher frequencies are found and attributed to the second and third cavity modes. Another notable finding is the weak sensitivity to ΔT which is the result of the relatively soft in-plane boundary restraint.

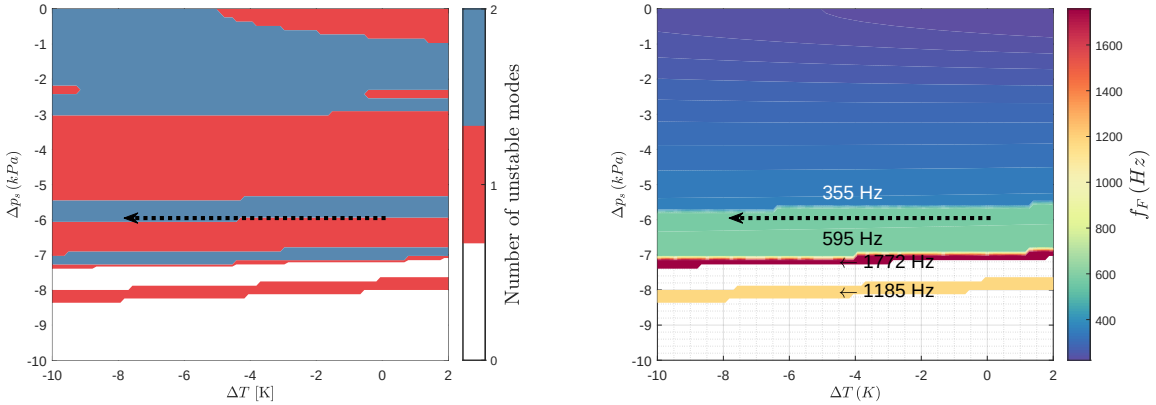

Figure 6: Stability diagram in Δp_s vs. ΔT plane showing (a) the number of unstable modes and (b) the frequency of the most unstable mode. A dashed arrow shows the wind tunnel conditions trajectory.

Figure 7 shows the modal frequencies of the plate and cavity versus ΔT at wind tunnel conditions for two configurations: (a) with and (b) without coupling between the plate and cavity dynamics. The figure shows that without coupling, the plate remains stable for all ΔT values. However the coupled solution predicts two modes of instability:(1) first and second structural mode coalescence and (2) third structural and first cavity mode coupling at 375 Hz and 590 Hz respectively. It is found that for all values of Δp_s in the range of interest, cavity coupling is necessary for instability of both types. To reach flutter onset without cavity dynamic coupling (and with added stiffness due to static deformation) at the wind tunnel test conditions, a significantly higher freestream static pressure of $p_\infty = 104kPa$ is required (4 times that of the wind tunnel freestream flow limit at Mach 2.5).

4.2 LCO amplitude sensitivity to static pressure differential

Figure 8 shows the normalized aerodynamic pressure rms at the plate center in a transient solution in which the static pressure differential is increased and decreased. In this computation, the temperature differential is held constant at $-4K$. The results show the sensitivity of the post-flutter LCO response amplitude of aerodynamic pressure to static pressure differential. The figure also shows the range of aerodynamic pressure rms measured with PSP (dashed red lines) which visualizes that some values of Δp_s may provide reasonable correlation between computational and experiment results. The figure emphasizes that the direct use of the wind tunnel conditions, which are the mean conditions over the test duration, are not likely to result in good

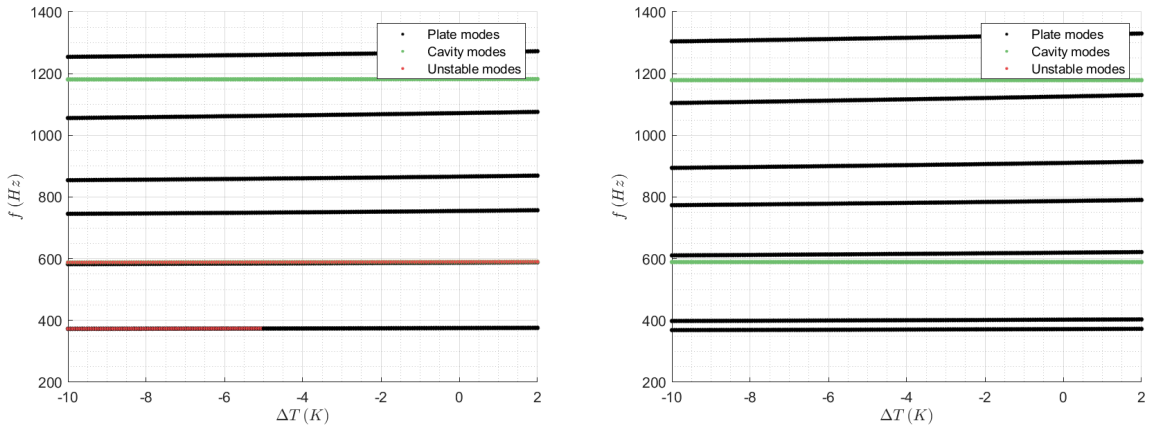

(a) (b)

Figure 7: Modal frequency vs. ΔT of plate, freestream, and cavity system for two configurations (a) with and (b) without plate-cavity coupling, calculated for wind tunnel conditions ($\Delta p_s = -6kPa$). Black: plate modes (stable), green: cavity modes (stable), red: unstable modes.

agreement between theory and experiment due to significant sensitivity to these parameters.

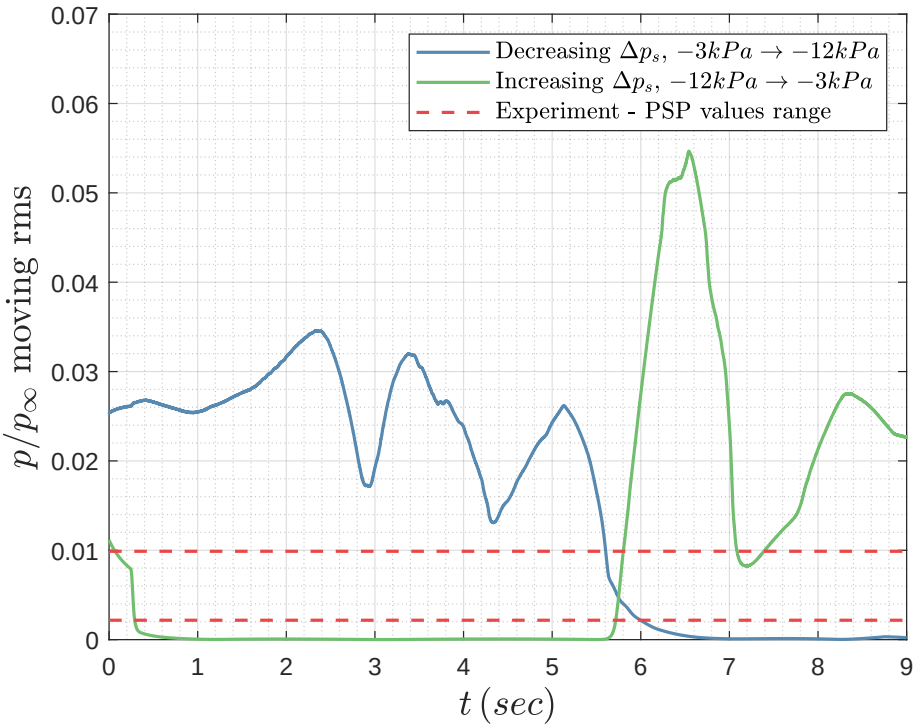

Figure 8: Computed moving-rms of pressure at the plate center vs. time using PF aerodynamics during static pressure differential increase and decrease (at a rate of $\pm 1kPa/sec$). Experiment - range of values from PSP are shown with red dashed lines.

Figure 9 shows the computed displacement at the plate center and the STFT of the aerodynamic pressure during an increase and decrease of Δp_s. The figures show that, as predicted by the linear stability analysis, transition between different modes of instability and participating modes is observed. Hysteresis in the transition between stable and unstable states is observed similar to that in [10]. Also note that the frequency content shows that the coalescence flutter around 350

Hz appears simultaneously with the cavity mode around 600 Hz in this range of parameters. This in contrast to the experimental measurements which did not show signs of cavity mode participation (see Figure 5).

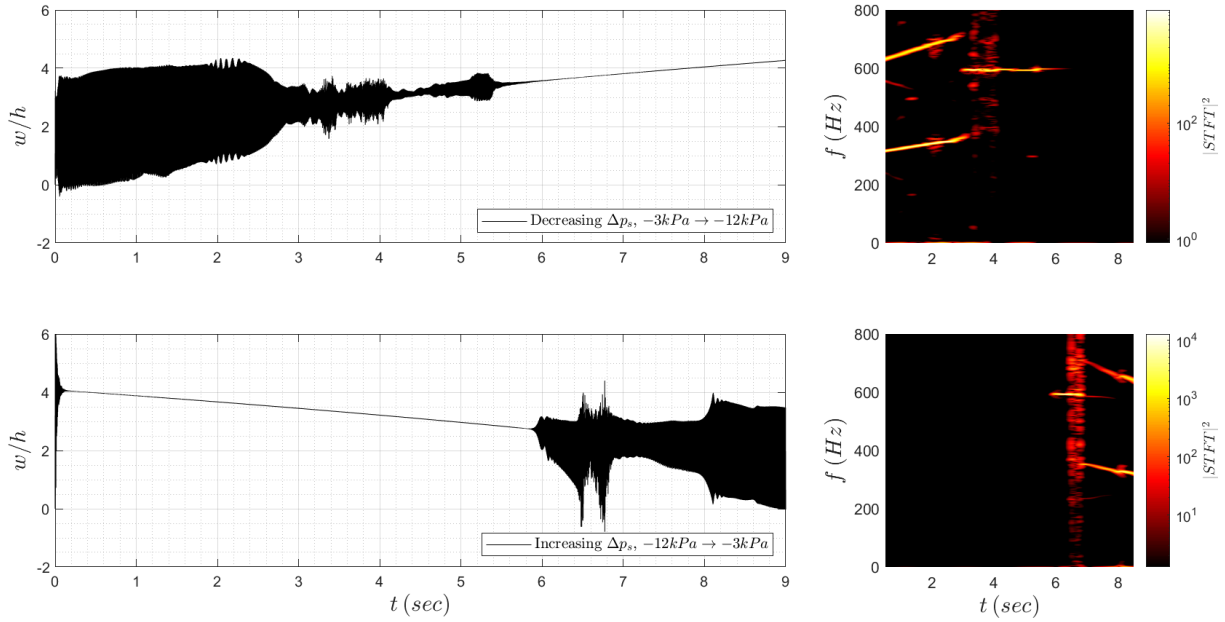

Figure 9: Left column: displacement at the plate center vs. time using PF aerodynamics during static pressure differential increase and decrease (at a rate of $\pm 1kPa/sec$), right column: aerodynamic pressure frequency content vs. time (STFT) at the plate center.

4.3 Transient response: aerodynamic pressure and displacement

In the next set of results the static pressure differential, Δp_s, is held constant at values close to the mean value inside the wind tunnel while the temperature differential, ΔT, is decreased at a rate of $-1K/sec$ starting from zero. This simulates the dynamics of these parameters inside the wind tunnel and makes this a direct correlation with the experiment. For each set of results, two aerodynamic models are considered, LPT and PF. For a dominant frequency of 325 Hz measured in the experiment, the reduced frequency is $\omega \cdot a/U_\infty \approx 1$ and the Mach number is 2.5. In these conditions PF is expected to provide more accurate results over LPT [3, 20].

Figure 10 shows the moving mean and moving rms of displacement at the plate center versus time for the duration of 8 seconds using PF aerodynamics and different values of Δp_s. It is shown that the relatively small change in Δp_s may lead to significant qualitative difference in the transient response as highlighted by the results for $\Delta p_s = -6kPa$. Both the mean and rms of the response decrease over time due to ΔT decrease. Figure 11 shows the same results obtained using LPT aerodynamics. With LPT, the response with $\Delta p_s = -6kPa$ is smooth like the other three cases. In addition, the response rms is increasing with decreasing ΔT over time, which is in contrast to results obtained with PF.

Figures 12 and 13 show the transient response for different values of Δp_s obtained with PF and LPT, respectively. Both sets of figures show the normalized displacement at the plate center and the STFT of the aerodynamic pressure at the same location. The STFT plots with both aerodynamic models show that instability at the lower frequency of 350 Hz is dominant at Δp_s of -4.5 kPa and -5 kPa. As Δp_s decreases, the response becomes dominated by the plate-cavity

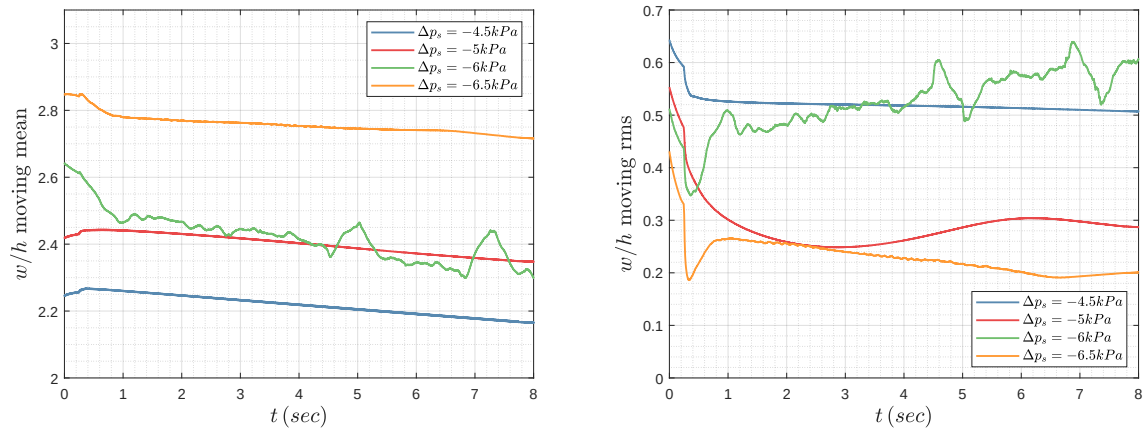

(a) (b)

Figure 10: (a) Moving-mean and (b) moving-rms of displacement at the plate center vs. time, with PF aerodynamics, constant static pressure differential, and decreasing temperature differential (at a rate of $-1K/sec$).

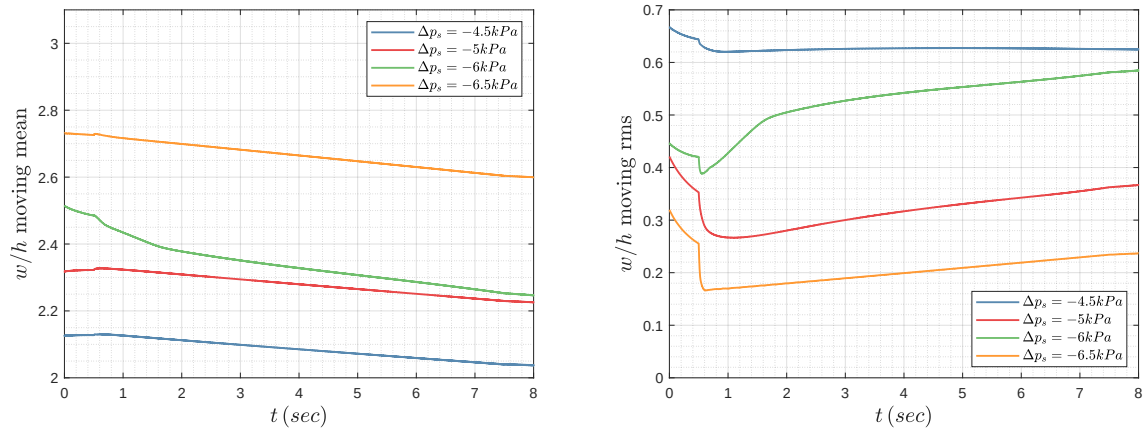

(a) (b)

Figure 11: (a) Moving-mean and (b) moving-rms of displacement at the plate center vs. time, with LPT aerodynamics, constant static pressure differential, and decreasing temperature differential (at a rate of $-1K/sec$).

resonance at 600 Hz. With PF aerodynamics and $\Delta p_s = -6kPa$, a non-periodic response is obtained. Overall computations with PF predict that as ΔT decreases, LCO amplitude should decrease. This is in contrast to LPT that predicts an increase in LCO amplitude.

Figures 14(a) and 14(b) show the moving rms of pressure at the plate center obtained with PF and LPT, respectively. Similar to the displacement response, the two aerodynamic models disagree on the dynamics with respect to the decrease in ΔT over time. With PF aerodynamics pressure rms remains relatively constant while LPT shows a smooth increase over time. The figures also show the pressure rms measured in the experiment. The curve that shows the experimental results was calculated by first detrending the PSP measurements, then calculating the moving window rms and normalizing it by the same moving mean of the same time window. This reduces uncertainties in freestream flow static pressure and the PSP calibration curve. Overall, theory and experiment agreement is reasonable considering the high sensitivity to Δp_s.

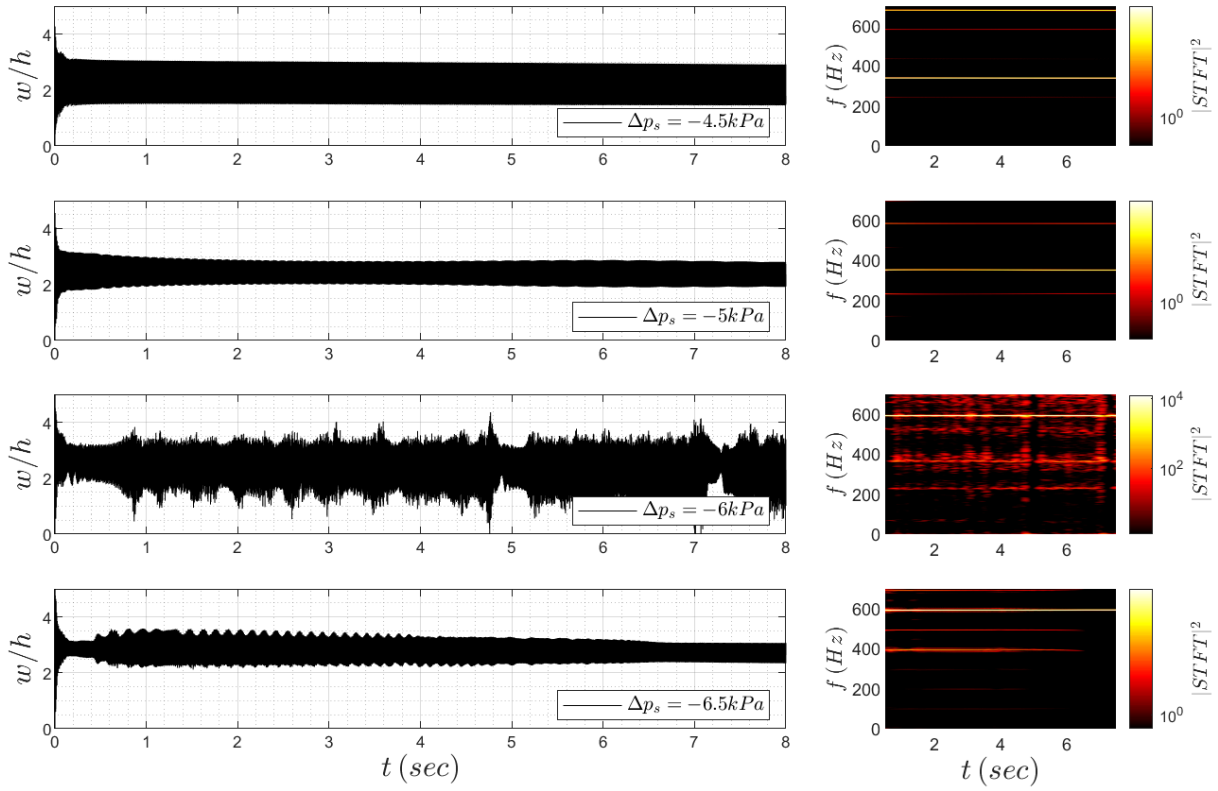

Figure 12: Left column: displacement at plate center vs. time for pinned boundary conditions with PF aerodynamics, constant static pressure differential, and decreasing temperature differential (at a rate of $-1K/sec$), right column: pressure frequency content vs. time (STFT) at the plate center.

4.4 Transient response: piezoelectric element voltage

So far, the transient response was investigated through the displacement and aerodynamic pressure at the plate center where direct correlation between computation and experiment was presented only for the latter. In Figure 15 the moving mean and moving rms of voltage on the downstream piezoelectric patch is shown for different values of Δp_s. On Figure 15(a) the moving mean of the measured voltage is shown after amplification by a factor of 40 to bring the values to a visible range when compared to computations. While the relation in Equation 11 relates modal displacement of the plate to the theoretical voltage of the piezoelectric element, the scaling coefficient may vary significantly due to the signal conditioning system. More generally, the signal conditioning system introduces a transfer function between deformation and the voltage output which, for accurate measurements, requires calibration over a range of frequencies of interest [23].

To utilize the voltage measurements without calibration, voltage moving rms values in Figure 15(b) are normalized by the instantaneous value of the moving mean. This is expected to remove dependency on the scaling factor while the potentially complicated behavior with respect to frequency is assumed to have a minor effect. Agreement between the computed and measured moving rms values show reasonable agreement similar to the pressure correlation in Figure 14.

4.5 LCO mode shape extraction

The spectral proper orthogonal decomposition (SPOD) [24] is used to extract the spatial mode shapes of the LCO from measurements and computed aerodynamic pressure. SPOD is com-

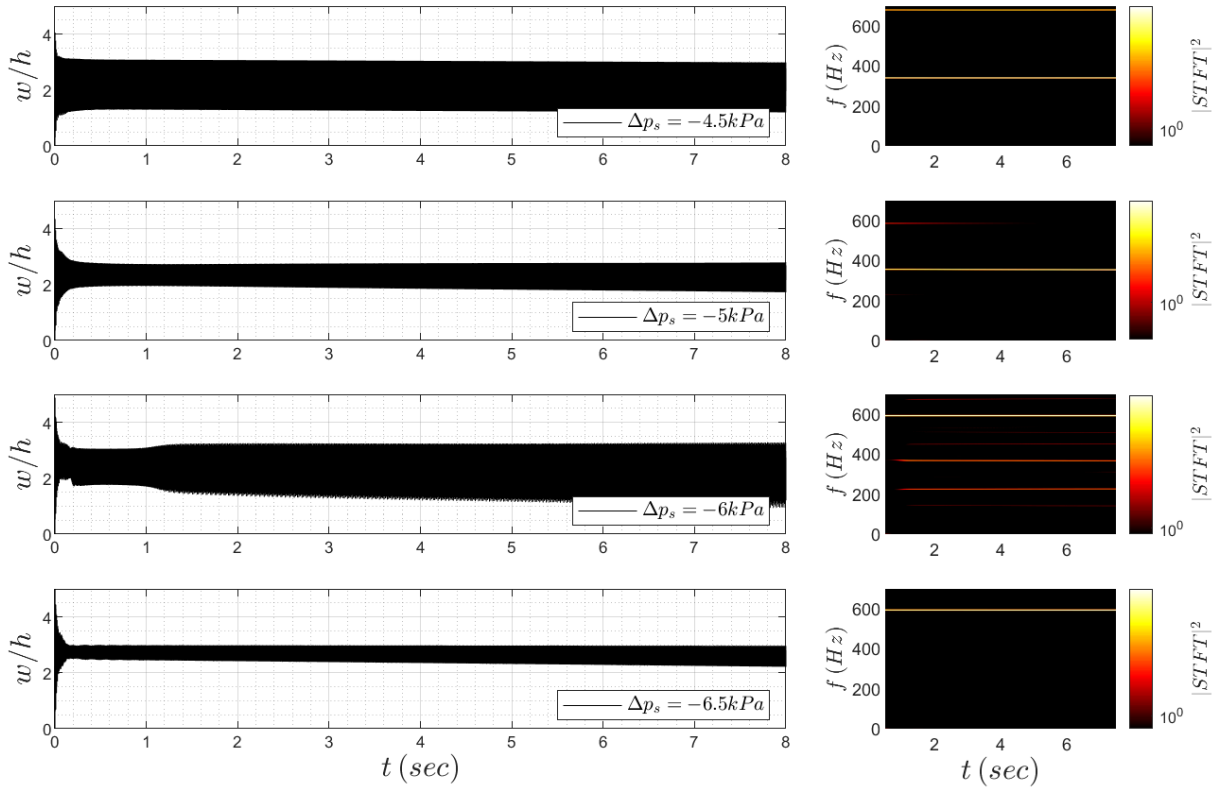

Figure 13: Left column: displacement at plate center vs. time for pinned boundary conditions with LPT aerodynamics, constant static pressure differential, and decreasing temperature differential (at a rate of $-1K/sec$), right column: pressure frequency content vs. time (STFT) at the plate center.

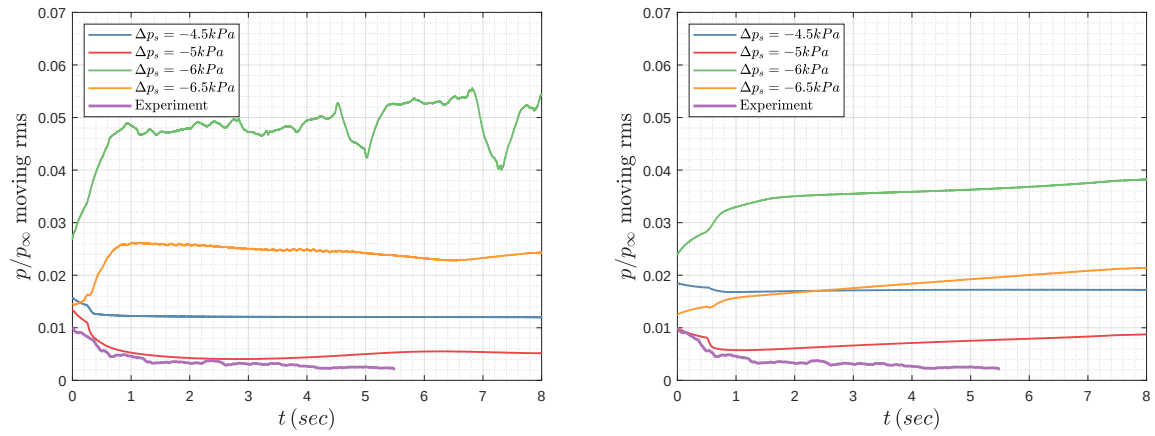

(a) (b)

Figure 14: Moving-rms of pressure at the plate center vs. time. Computational results with (a) PF and (b) LPT aerodynamics, constant static pressure differential, and decreasing temperature differential (at a rate of $-1K/sec$).

puted using 85 chordwise and 25 spanwise points in the PSP measurement field. A signal of 4 seconds is used from both the experiment and computation after skipping the first second of data to the skip the transient phase. Each point signal is processed by subtracting a linear best fit curve (detrend). SPOD is applied on signals sampled at 20 kHz using a window size of 0.25 seconds and overlap of 0.225 seconds.

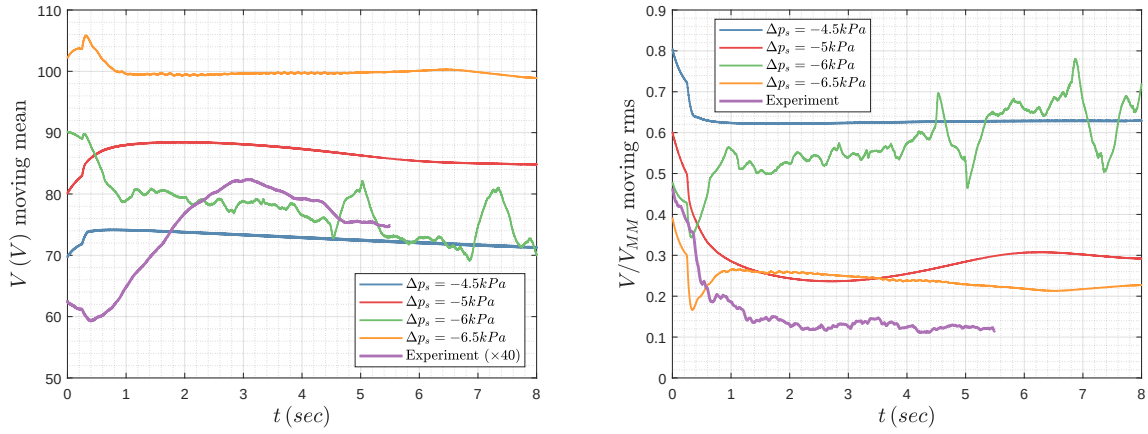

(a) (b)

Figure 15: (a) Moving-mean and (b) moving-rms (normalized by instantaneous moving-mean) of voltage computed and measured at the downstream piezoelectric element vs. time. Computational results with PF aerodynamics, constant static pressure differential, and decreasing temperature differential (at a rate of $-1K/sec$).

Figure 16 shows the SPOD spectra for the experimental PSP data. The first eigenvalue is dominant and shows peaks around 350 Hz and smaller peaks around 1150 Hz which is near the theoretical frequency of the cavity second mode. No significant peak is observed at the first cavity mode around 600 Hz. In contrast to the STFT in Figure 5(a) which is applied to a signal at a single point (plate center), the SPOD uses multiple points and captures dynamics at a significantly wider range of frequencies. Figure 17 shows the mode shapes corresponding to peak values at 324 Hz and 386 Hz. It is important to note that in post-flutter oscillation, the structural response of a plate is nonlinear and the LCO is not necessarily periodic in time. This means that the LCO mode shape might not have a simple representation using the fundamental modes of a flat plate. The mode shape appears to show more participation at the trailing edge than the leading edge with participation of up to the 5th chordwise mode. However at this point its important to emphasize that these mode shapes are the aerodynamic pressure and not the structural mode shapes. To clarify the difference between the two, consider Equation 4 where the aerodynamic stiffness term is expected to be dominant at Mach 2.5 and in physical coordinates it is a function of the local chordwise slope, $\frac{\partial w}{\partial x}$. Now consider the shape of the first chordwise mode and notice that the spatial shape of its chordwise derivative has negative and positive sides making it appear as a higher order mode. A similar effect is observed in Figure 17 where it is likely that the structural mode participating here is the 4th mode. Also, some asymmetry in the spanwise direction is observed in Figure 17(b).

Figure 18 shows the SPOD spectra for the computed solution with PF aerodynamics and two values of Δp_s. Figure 12 showed that a value of $\Delta p_s = -5kPa$ leads to a periodic LCO while the lower value of $\Delta p_s = -6kPa$ leads to a nonperiodic LCO. This qualitative difference is also shown through the SPOD spectra for the two cases. In contrast to the experimental data, a wide range of peak frequencies is found in the range of up to 2000 Hz. Peak frequencies near 350 Hz are selected and the corresponding mode shapes are shown in Figure 19.

5 CONCLUSION

The post-flutter LCO response of an elastic plate in Mach 2.5 flow was investigated computationally and correlated with experiment. The structural computational model was extended to

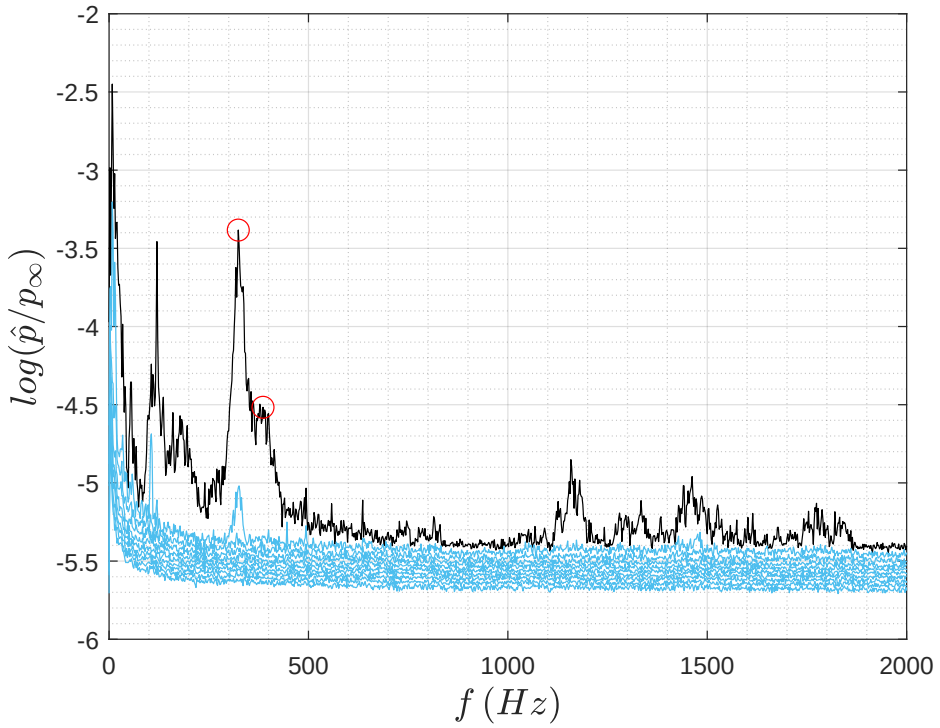

Figure 16: SPOD spectra for the pressure sensitive paint experimental data. The black line shows the dominant eigenvalue spectra which is used to extract the spatial mode shapes at two peak values as shown by the two red circles. The rest of the lines show spectra of higher order eigenvalues.

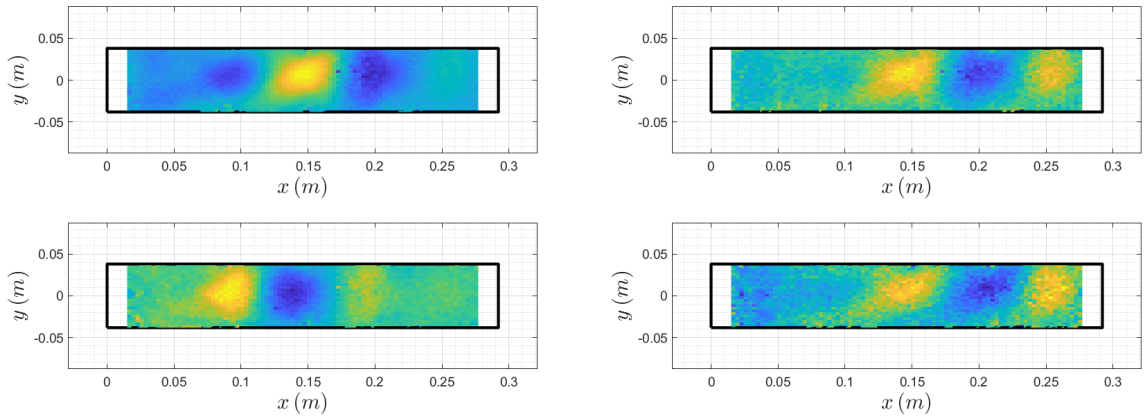

(a) (b)

Figure 17: Experiment - SPOD extracted mode shapes (of aerodynamic pressure) at peak frequencies of (a) $324Hz$ and (b) $386Hz$, top and bottom rows show the real and imaginary parts, respectively.

include more detailed in-plane boundary conditions by adding rivet connection elasticity and a sensitivity study for the static pressure differential was conducted. Full-field measurements of pressure were used to correlated with computed aerodynamic pressure using two aerodynamic models of different levels of complexity and accuracy. The measured voltage on a thin elastic piezoelectric patch was used to study the structural response and correlated computation with experiment. The following conclude the key findings of the present study.

1. Plate connection to the supporting structure using rivets was found to be important to

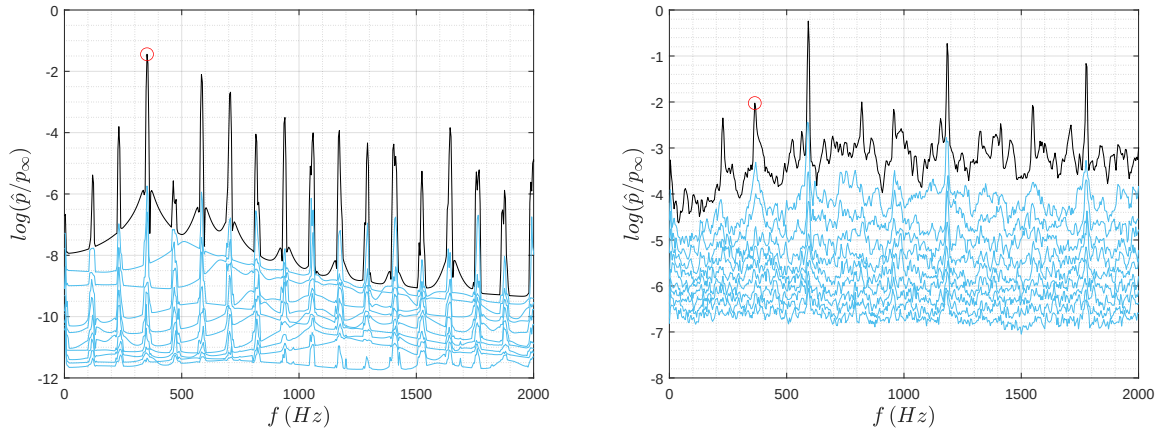

(a) (b)

Figure 18: SPOD spectra of pressure for computational solutions obtained for (a) $\Delta p_s = -5kPa$ (periodic LCO) and (b) $\Delta p_s = -6kPa$ (nonperiodic LCO) cases with PF aerodynamics and decreasing temperature differential. Peak values are shown in red circle and are used to extract the dominant spatial mode shape.

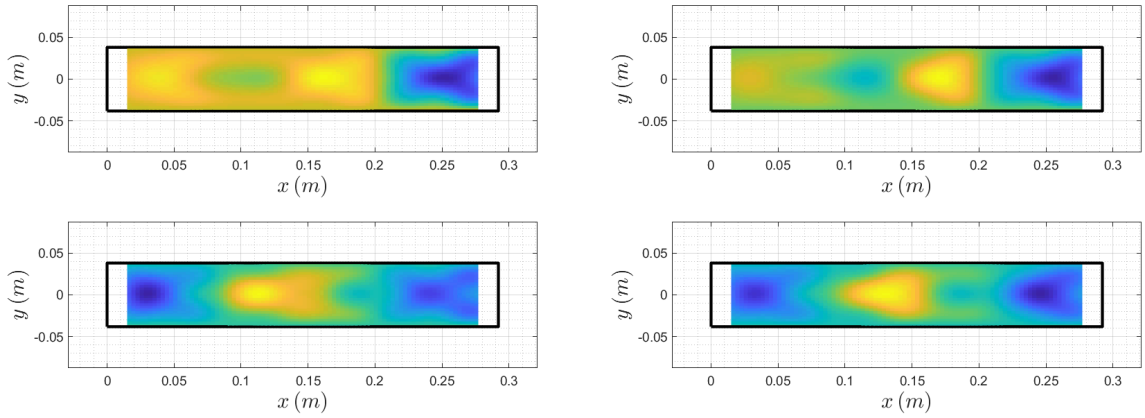

(a) (b)

Figure 19: SPOD extracted mode shapes (of aerodynamic pressure) at peak frequencies for (a) $\Delta p_s = -5kPa$ ($352Hz$) and (b) $\Delta p_s = -6kPa$ ($364Hz$) cases with PF aerodynamics and decreasing temperature differential. Top and bottom rows show the real and imaginary parts, respectively.

the nonlinear structural stiffness. The change in natural frequency of a plate under a static load is sensitive to the level of restraint at the edges. Subsequently, the change in natural frequencies of the structure is important for the aeroelastic stability and post-flutter response. Rivets were found be closer to free in-plane boundary conditions than fixed however their discrete spatial distribution impacts each structural mode differently.

2. An eigenvalue stability analysis showed that the dynamic coupling between cavity pressure, plate, and freestream flow is essential for flutter onset under the studied conditions. This is a surprising result considering previous works suggesting limited cavity effect on aeroelastic stability [10].
3. The transient post-flutter LCO aerodynamic pressure and displacement response were investigated computationally and correlated with experiment. Potential flow aerodynamics showed non-priodic LCO which agrees better with experiment while Piston Theory aerodynamics result in periodic LCO. Significant sensitivity to static pressure differential

was found using both aerodynamic models which suggests that direct correlation between theory and experiment is a challenging task near the flutter envelop.

4. SPOD was used to analyze the frequency content and extract the spatial shape (distribution) of the aerodynamic pressure during LCO. The decomposition was applied on measured and computed pressure and in both cases the spatial shapes showed the participation of up to the 4th chordwise modal shape.

FUNDING SOURCES

This work was supported in part by U.S. Air Force Office of Scientific Research with Drs. Sarah Popkin and Martin Schmidt as Program Directors.

6 REFERENCES

[1] Eason, T., Spottswood, S. M., and Chona, R. (2013). A structures perspective on the challenges associated with analyzing a reusable hypersonic platform. In *11th International Conference on Recent Advances in Structural Dynamics*. University of Pisa, Italy.

[2] McNamara, J. J. and Friedmann, P. P. (2011). Aeroelastic and aerothermoelastic analysis in hypersonic flow: Past, present, and future. *AIAA Journal*, 49(6), 1089–1122.

[3] Dowell, E. H. (1974). *Aeroelasticity of plates and shells*. Noordhoff International Publishing (now Springer).

[4] Spottswood, S. M., Beberniss, T. J., Eason, T. G., et al. (2019). Exploring the response of a thin, flexible panel to shock-turbulent boundary-layer interactions. *Journal of Sound and Vibration*, 443, 74 – 89. ISSN 0022-460X. doi:https://doi.org/10.1016/j.jsv.2018.11.035.

[5] Varigonda, S. V., Serafim, L. P., Freydin, M., et al. (2024). Two-dimensional pressure field imaging of an elastic panel executing post-flutter oscillations. *Journal of Fluids and Structures*, 125, 104056. ISSN 0889-9746.

[6] Hess, R. W. (1970). Experimental and analytical investigation of the flutter of flat built-up panels under streamwise inplane load. *NASA TR R-330, Langley Research Center*.

[7] Kappus, H., Lemley, C., and Zimmerman, N. (1971). An experimental investigation of high amplitude panel flutter. *NASA CR-1837*.

[8] Dowell, E. H. and Voss, H. M. (1965). Theoretical and experimental panel flutter studies in the mach number range 1.0 to 5.0. *AIAA Journal*, 3(12), 2292–2304. doi:10.2514/3.3359.

[9] Daub, D., Willems, S., and Gülhan, A. (2022). Experiments on aerothermoelastic fluid–structure interaction in hypersonic flow. *Journal of Sound and Vibration*, 531, 116714. ISSN 0022-460X. doi:https://doi.org/10.1016/j.jsv.2021.116714.

[10] Freydin, M., Dowell, E. H., Spottswood, S. M., et al. (2021). Nonlinear dynamics and flutter of plate and cavity in response to supersonic wind tunnel start. *Nonlinear Dynamics*, 103(4), 3019–3036.

[11] Brouwer, K. R., Perez, R. A., Beberniss, T. J., et al. (2021). Experiments on a thin panel excited by turbulent flow and shock/boundary-layer interactions. *AIAA Journal*, 59(7), 2737–2752. doi:10.2514/1.J060114.

[12] Brouwer, K. R., Perez, R. A., Beberniss, T. J., et al. (2022). Evaluation of reduced-order aeroelastic simulations for shock-dominated flows. *Journal of Fluids and Structures*, 108, 103429. ISSN 0889-9746. doi:https://doi.org/10.1016/j.jfluidstructs.2021.103429.

[13] Brouwer, K. R., Perez, R. A., Beberniss, T. J., et al. (2023). Aeroelastic response of a thin panel excited by a separated shock–boundary layer interaction. *Physics of Fluids*, 35(12), 125153. ISSN 1070-6631. doi:10.1063/5.0175161.

[14] Currao, G. M. D. and He, H.-C. (0). Transonic flutter of skin panels pinned at the center. *AIAA Journal*, 0(0), 1–15. doi:10.2514/1.J063735.

[15] Whalen, T. J., Kennedy, R. E., Laurence, S. J., et al. (2019). Unsteady surface and flow-field measurements in ramp-induced turbulent and transitional shock-wave boundary-layer interactions at mach 6. In *AIAA Scitech 2019 Forum*. doi:10.2514/6.2019-1127.

[16] Eitner, M. A., Ahn, Y.-J., Musta, M. N., et al. (2023). Vibration of a thin panel exposed to ramp-induced shock-boundary layer interaction at mach 2. *Journal of Fluids and Structures*, 119, 103894. ISSN 0889-9746. doi:https://doi.org/10.1016/j.jfluidstructs.2023.103894.

[17] Daub, D., Willems, S., and Gülhan, A. (2016). Experiments on the interaction of a fast-moving shock with an elastic panel. *AIAA Journal*, 54(2), 670–678. doi:10.2514/1.J054233.

[18] Gramola, M., Bruce, P. J., and Santer, M. J. (2020). Response of a 3d flexible panel to shock impingement with control of cavity pressure. In *AIAA Scitech 2020 Forum*. doi:10.2514/6.2020-0314.

[19] Freydin, M. and Dowell, E. H. (2021). Nonlinear theoretical aeroelastic model of a plate: Free to fixed in-plane boundaries. *AIAA Journal*, 59(2), 658–672. doi:10.2514/1.J059551.

[20] Serafim, L. P., Freydin, M., and Dowell, E. H. (2023). Flutter and limit-cycle oscillations of a panel using unsteady potential flow aerodynamics. *AIAA Journal*, 61(11), 5009–5017. doi:10.2514/1.J062943.

[21] Dowell, E. H. and Bliss, D. B. (2013). New look at unsteady supersonic potential flow aerodynamics and piston theory. *AIAA Journal*, 51(9), 2278–2281. doi:10.2514/1.J052088.

[22] Freydin, M., Dowell, E. H., Varigonda, S. V., et al. (2022). Response of a plate with piezoelectric elements to turbulent pressure fluctuation in supersonic flow. *Journal of Fluids and Structures*, 114, 103696. ISSN 0889-9746. doi:https://doi.org/10.1016/j.jfluidstructs.2022.103696.

[23] Sirohi, J. and Chopra, I. (2000). Fundamental understanding of piezoelectric strain sensors. *Journal of intelligent material systems and structures*, 11(4), 246–257.

[24] Towne, A., Schmidt, O., and Colonius, T. (2018). Spectral proper orthogonal decomposition and its relationship to dynamic mode decomposition and resolvent analysis. *Journal of Fluid Mechanics*, 847, 821–867.

COPYRIGHT STATEMENT